RESEARCH ARTICLE

COLOR RESEARCH AND APPLICATION | WILEY

Efficient nucleus segmentation of white blood cells mimicking the human perception of color

Farid García-Lamont[1] 🆔 | **Matías Alvarado**[2] | **Asdrúbal López-Chau**[3] |
Jair Cervantes[1]

[1]Centro Universitario UAEM Texcoco, Universidad Autónoma del Estado de México, Texcoco, Estado de Mexico, Mexico

[2]Centro de Investigación y de Estudios Avanzados del IPN, Departamento de Computación, CDMX, CDMX, Mexico

[3]Centro Universitario UAEM Zumpango, Universidad Autónoma del Estado de México, Zumpango, Estado de Mexico, Mexico

Correspondence
Farid García-Lamont, Centro Universitario UAEM Texcoco, Universidad Autónoma del Estado de México, Av. Jardín Zumpango s/n, Fraccionamiento El Tejocote, CP 56259, Texcoco-Estado de México, México.
Email: fgarcial@uaemex.mx

Abstract

In this study, we present a nucleus segmentation proposal of white blood cells (WBCs) using chromatic features. It is human inspired on perception of color: a person locates the nucleus of the WBCs by the chromatic contrast between the nucleus and the other elements of the blood smear. To implement that, we segment the nucleus by selecting the pixels with high chromatic variance. First, an unsupervised neural network, which was trained offline to recognize different colors is applied to the images. Thereby, the hue of the pixels is normalized, and the chromatic variance is accurately computed. Processing the hue and using the unsupervised neural network the brightness and staining variations are robustly estimated. In previous related works, the color components are processed separately as uncorrelated intensity channels, and the mathematical operations are selected intuitively. Unlike that, we use color as a feature without separating the hue components, keeping their correlation, so the formal treat becomes systematic. Experiments use the RGB and HSV spaces with three public image databases: ALL-IDB2, CellaVision, and JTSC. A pixel-level segmentation evaluation is performed by comparing the segmented images with the ground truth. Our proposal competes with current methods since the values in accuracy, specificity, precision, sensitivity, dice coefficient, kappa index, and true positive rate all are similar to or improved upon the state of the art. The performance of our approach is classified as excellent regarding the kappa index value, and it detects at least 80% of the cells with an average dice coefficient larger than 0.9.

KEYWORDS
chromaticity, color recognition, color spaces, image segmentation, white blood cells

1 | INTRODUCTION

White blood cells (WBCs) or leucocytes are blood cells that actively participate in the human immune system to defend the body against invaders; when a person suffers from an infection, the immune system creates more WBCs to defend the body[1,2,3]. An increased number of WBCs is relevant factor to determine if the body is being infected. Also, in leukemia cancer, abnormal WBCs proliferate and counting them is essential to diagnose this disease in a person. As well, it is essential to analyze the WBCs' nucleus features to provide information about unhealthy due to leukemia, despite the low number of WBCs.[4,5] The Global Cancer Observatory reported

474 519 new cases and 311 594 deaths in 2020.[6] There-fore, it is pertinent an agile diagnose on cancer stage of deploy that the WBCs nucleus segmentation and late automated recognition and counting helps to contribute to progress in the scope of this computational diagnosis medicine.

The detection and analysis of WBCs are traditionally performed from blood sample extracted from the patient. The WBCs are stained to become visible, a hematologist analyzes the sample, and from the results reported the doctors provide a diagnosis. The analysis process frequently is slow because it is not automated; also, the analysis may be affected by the fatigue level and experience of the hematologist, with involuntary errors or misreports. Several related works focus onto study the nucleus features of the WBCs to provide important data to detect major types of leukemia.[7] Therefore, the development of algorithms for nucleus segmentation is an active research area within image processing that contributes with the automated analysis of the WBCs.[7] In artificial vision systems for WBCs nucleus analysis, the usual stages are: (a) image acquisition, (b) image preprocessing, (c) nucleus segmentation, (d) feature extraction, and (e) classification.[8] In this study, we present an efficient WBC's segmentation proposal on the base of the nucleus segmentation quality, a feature extraction that is highly discriminative. The nucleus segmentation implies challenges such as hue variations and brightness variations, because of the staining procedures and illumination. The shape of the nucleus, the magnification, and the cameras employed to acquire the images should be considered in a further analysis—beyond the scope in this work.

Previous works on nucleus segmentation of WBCs employ: convolutional deep learning,[1,9] image descriptors,[9,10] convolutional neural networks,[11-14] geometric active contours,[15] spectral signatures,[16,17] among other techniques.[18-31] Most related works that use color information to segment WBCs do not use color as a feature, since mathematical operations are performed on the color components separately as intensity channels, and, the color components are intuitively chosen.[27,32-42] However, it means that through all chromaticity is not properly processed.

We propose the color processing as a sole feature for segmentation. Our proposal mimics the human perception of color that recognizes colors first by the chromaticity and then by the intensity. For instance, in Figure 1, it is easy to appreciate that the color of squares (A) and (B) is green; even square (A) is brighter than square (B) the chromaticity does not change; nevertheless, any person learns that squares (A) and (B) are the same color with different intensities. Any person can claim that the color of square (C) is red, and of square (D) is pink, and
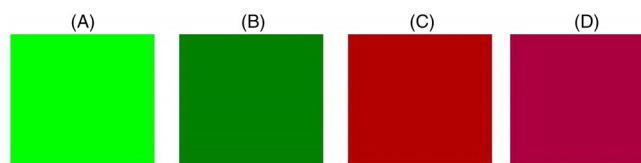

FIGURE 1 Squares (A) and (B) with the same chromaticity but different intensity; squares (C) and (D) with different chromaticity with the same intensity

that the intensity of both squares is the same. Despite the chromaticity difference between both squares is small, any person can notice that the hues of squares (C) and (D) are not the same, although the intensity is equal.

Once the WBCs are stained, the nuclei are easy to locate within the blood smear by any person, because the color of the WBCs contrasts regarding the color of the other elements of the blood smear. Specifically, what a person identifies is the chromatic difference of the elements within the image.

Brief overview of our proposal for the nucleus segmentation of WBCs using chromatic features of the blood smear follows. The nucleus of the WBCs is segmented by selecting the pixels whose chromatic variance is high. Before the chromatic variance is computed, the hues of the image are normalized by preprocessing the input images with an unsupervised neural network (NN). This NN is trained offline with representative hue samples, such that each neuron of the NN learns to recognize a specific hue. When the image is preprocessed by the NN, the chromaticity of the pixels is substituted by the hue the winning neuron learned to recognize; thereby, certain robustness to staining variations is achieved and the computing of chromatic variance increased precision. Besides, by processing the images just by chromatic features, the robustness of brightness variation is obtained to some extent.

We use the HSV space because the color representation emulates the human perception of color,[43] since the chromaticity and the intensity are decoupled for color processing.[43-47] Note the selection of pixels whose chromatic variance is high regarding the hue of the other elements of the blood smear. The RGB color space is often employed for color processing because of its sensitivity to non-uniform illumination,[44-46] despite it is not adequate for color processing; the RGB space can be used because the images are acquired under controlled illumination conditions. Therefore, we experimented with both color spaces and then compared the results obtained.

Previous works that use color data for segmentation do not use it as a feature and perform mathematical operations in the color components separately, like intensity channels, so color components are uncorrelated.

Furthermore, the color components and the mathematical operations are selected intuitively. In our proposal, the hue components are processed as a sole feature without separating them, keeping the correlation of the color components, so it allows a formal systematic treatment.

The rest of the article is organized as follows: works addressing the segmentation of WBCs using color information are reviewed in Section 2; we present our segmentation approach in Section 3, and the experiments and metrics to evaluate its performance thru well-known databases in Section 4. Discussion on the results and extensive analytical comparison is in Section 5. The article closes with Conclusions in Section 6.

2 | PREVIOUS WORKS

Challenges to segmentation of WBCs in an image are that cells have many variations in shapes, the sizes of the images are not equal, and illumination conditions frequently vary, among other factors. Previous works use color information represented in models of RGB, HSI, CIELAB, among others. One of the main steps to segment WBCs in images is to locate them precisely.

In reference 19, a set of sliding windows is used along with a metric to identify the best window that contains a WBC; metric combines the density of edges using the Canny with the colors of WBCs. To segment a WBC in an image, a combination of GrabCut algorithm and dilatation is applied.

Prinyakupt et al.[27] highlight the nucleus by the sum of the R and B channels of the RGB space, and the result is divided by the value of channel G. The histogram equalization is applied, and the image is binarized and used to segment the nucleus; then to remove noise and fill gaps, morphological dilation is applied to a disc-shaped structure to join segmented nucleus with the lobes.

In reference 29, the input image is mapped to the HSV color space; data are divided in four k-means clusters involving the H and S components; nuclei are segmented by selecting the cluster with the lowest red value. In reference 32, the WBC area is obtained by converting the input image to the HSI color space, k-means clustering is applied to the H component, followed by the median filter and region growing algorithm. The image containing the WBC is employed to obtain the nucleus area, with the S component treated similar. In reference 33, convert the input to grayscale binarized image (Otsu method), morphological operators are applied by a disc-shaped structure; the connected components with an axis length 30% smaller than the average are removed from the binary image. In reference 34, a color correction process using CIELAB color space is made manually; then,

red blood cells and background using Otsu thresholding and combination of RGB, CMYK, and HSV color space analysis are applied to segment WBCs; the noise is removed using a morphological filter and connected component labeling. Circle Hough Transform is applied to detect overlapped cells.

Cao et al.[35] use the low-rank representation (LRR) method to capture the underlying low-dimensional structures of high-dimensional data. LRR finds a small set of vectors that represent the data as a linear combination of them, then detecting first the area of WBC by the optimal thresholding technique. In reference 37, a method where the R and G components are replaced from the input color image by normalized and contrast enhanced G component; this increases the contrast between the region of nuclei and the background.

In reference 39, the noise of the RGB input image is removed using a median filter and a Gaussian filter; the resulting image is mapped to the CIELAB color space; then, the chromatic components a^* and b^* are used to divide the image into three k-means groups. Nucleus is segmented by selecting the cluster with the highest intensity of component a^* and lowest component of b^*. In reference 40, the input RGB image is mapped to the HSV image; from the S component, the borders are obtained with the gradient method, the image is binarized by thresholding the gradient magnitudes. The proposed border strength location windows are processed with the Grabcut method.

Vogado et al.[41] convert the input image to the CMYK and CIELAB color spaces. The contrast of the M component and the b^* component is adjusted, a median filter is applied. The WBCs are enhanced by subtracting b^* from the component M. The k-means algorithm divides the resulting images into nucleus, cytoplasm, and background. Morphological operations erosion and dilation are applied.

In reference 42, the B and G channels are subtracted, negative values are set to zero; thereby, the WBCs are highlighted. The image is binarized with the Otsu method and then active contouring is applied. The binary image is transformed into a distance map by computing the minimum Euclidean distance between the pixels of the nucleus area and the background. The map is used to define markers, where the watershed algorithm is employed to delimit the area of the nucleuses.

3 | SEGMENTATION PROPOSAL

Our proposal to process the hue, keeping the correlation between their components, emulates the human perception to recognize colors, first by the chromaticity and

then by the intensity. A person, by means of color, easy can locate the nucleus of the WBCs, detecting the hue contrast between the nucleus and the other elements of the blood smear. We segment the nucleus by selecting the pixels with high chromatic variance regarding the components of the blood smear, an easy to implement approach for WBC segmentation. Also, we use an unsupervised NN trained offline with representative samples of different hues, such that each neuron learns to recognize a specific hue or chromaticity. The pixels are processed using the NN, and their chromaticity is substituted by the weight vector of the respective winning neurons; thus, to recognize, the hue of the winning neurons is learned. The NN usage is twofold, to normalize the chromaticity of the pixels and to reduce the staining variations. As a result, computing the chromatic variance of the pixels earned accuracy. Figure 2 shows a flowchart summarizing our proposal. The red component of the colors is set to zero to enhance the hue of the nucleus. Utilizing the NN, the resulting image is processed with the reduced number of hues. Finally, the chromatic variance of the pixels is computed to segment the nucleus of the WBC.

FIGURE 2   Flowchart of proposed approach

FIGURE 3   Images (A) and (B) show the RGB and HSV color spaces, respectively

3.1 | RGB and HSV color spaces

The representation of colors is significant to obtain a precise color characterization; the RGB space is often employed because most of the image acquisition hardware uses this space to represent colors. Nevertheless, the RGB space is not adequate for color processing because the color differences cannot be computed with the Euclidean distance since the intensity and chromaticity are not decoupled.[45]

However, considering that the images are acquired under controlled illumination conditions, it is possible to process the chromaticity. The RGB space is based on the Cartesian coordinate system, where colors are points defined by vectors that extend from the origin, see image (A) of Figure 3. The color of a pixel p is represented as:

$$\phi_p = \left[r_p, g_p, b_p \right] \tag{1}$$

Where r_p, g_p and b_p are the red, green and blue components of the color vector, respectively. The features of the color vectors are[45]:

1. The orientation represents the chromaticity.
2. The magnitude models the intensity.

The number of colors of the RGB space is infinite, but in the image processing field, the RGB space is
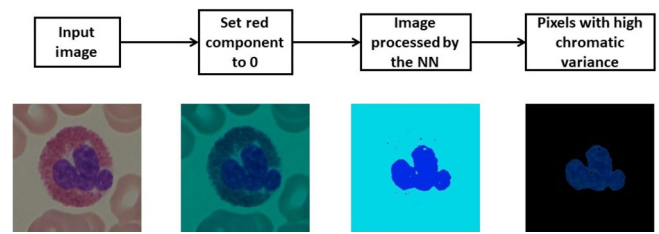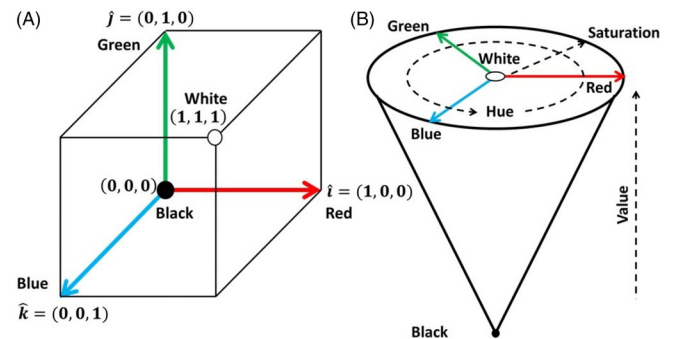
discretized; usually, the range of each component is $[0, 255] \subset \mathbb{Z}$. On the other hand, the HSV space is more suitable for color processing: the color representation in the HSV space resembles the human perception of color because the chromaticity is decoupled from the intensity.[43,45] The HSV space is cone-shaped, as shown in image (B) of Figure 3. The color of a pixel p in the HSV space has the components hue (h), saturation (s), and value (v), that is:

$$\varphi_p = \left[h_p, s_p, v_p \right] \tag{2}$$

h is the chromaticity, s is the distance to the axis of black-white, and v is the intensity; h is distributed through the circumference of the cone so in the range $[0, 2\pi] \subset \mathbb{R}$, $s \in [0, 1]$ interval and $v \in [0, 255]$. The mathematical operations to map colors between the RGB and HSV color spaces is given in reference 45.

3.2 | NN training

The unsupervised NN is trained such that each neuron learns to recognize a specific hue. The NN is fed with the hue of a pixel then the weight vector of the winning neuron substitutes the chromaticity of the given pixel. The number of hues the image can have is at most the number of neurons of the NN.

The training set is built with representative hue samples; for the RGB space, the reference 46 shows that hue samples of the inner faces of the RGB cube are representative enough to train the NN. The training set is built as follows, the elements of the set Θ are numbers 3 $n \in [0, 90]$ interval:

$$\Theta = \{3n \mid 0 \le n \le 30, n \in \mathbb{Z}\} \tag{3}$$

The sets S and C are built computing the sinus and cosine values of the elements of the set Θ respectively.

$$S = \{\sin\theta_k \mid \forall\theta_k \in \Theta\} \tag{4}$$

$$C = \{\cos\theta_k \mid \forall\theta_k \in \Theta\} \tag{5}$$

Using the Cartesian product, in the sets P_1, P_2, and P_3 we obtain the color vectors of the inner faces of the RGB cube for the planes R-G, G-B, and R-B, respectively.

$$P_1 = C \times S \times \{0\} \tag{6}$$

$$P_2 = \{0\} \times C \times S \tag{7}$$

$$P_3 = S \times \{0\} \times C \tag{8}$$

Finally, the training set P_ϕ is obtained with:

$$P_\phi = \bigcup_{i=1}^{3} P_i \tag{9}$$

While for the HSV space, reference 48 shows how the training set P_φ is built with:

$$P_\varphi = \left\{ [\cos\theta_k, \sin\theta_k] \mid \theta_k = \frac{\pi}{128}k : k = 0, 1, ..., 255 \right\} \tag{10}$$

For the experiments, we employ both competitive neural networks (CPNN) and self-organizing maps (SOM), trained offline using the Kohonen learning rule.[49]

Processing the image by NN can be regarded as a color clustering process. The advantages of using an NN, as we do, regarding clustering techniques such as k-means or fuzzy c-means, are that such techniques require a priori the number of groups the data (pixels) are grouped.[47] But the adequate number of groups changes depending on the image conditions. With the NN, the number of groups is variable with a limit at the largest number of colors the NN can recognize, in other words, the number of neurons of the NN.[47]

An important remark is that the clustering techniques usually create groups with the same size or

number of elements; for image segmentation, it implies that small parts within the image are not successfully segmented.[47] To overcome this restriction, we use a NN to segment small areas as each pixel is processed independently from the rest of the image. Also, the performance of the clustering techniques depends on the initial values of the centers. With the NN, after offline training, the NN can be used to process any image without training it again, unlike the clustering techniques.

3.3 | Algorithm

The steps of our proposal are next listed, we present how to process the colors represented in the RGB space but at the end of this section, we mention how to process HSV colors.

Let $\Phi = \{\phi_1, ..., \phi_m\} \subset \mathbb{R}^3$ be the set of RGB color vectors of the given image.

1. The red component of the color vectors is set to zero, $\phi_i^* = [0, g_i, b_i]$, then all vectors are included in the set $\Phi^* = \{\phi_1^*, ..., \phi_m^*\}$.
2. The vectors in the set Φ^* are normalized with $\hat{\phi}_i = \phi_i^* / \| \phi_i^* \|$, the resulting vectors form the set $\hat{\Phi} = \{\hat{\phi}_1, ..., \hat{\phi}_m\}$.
3. The NN is fed with the elements of the set $\hat{\Phi}$, the weight vectors $\mathbf{w}_k$ of the winning neurons are obtained with:

$$\mathbf{w}_k = \arg \max_{\mathbf{w}_i} \left(\mathbf{w}_i \cdot \hat{\phi}_p \right) \tag{11}$$

That is, the NN is excited with each element of the set $\hat{\Phi}$ and the respective weight vector of the winning neuron is placed in the set $W = \{\mathbf{w}_1, ..., \mathbf{w}_m\}$.

4. The variance of the elements of the set W is obtained as follows. The average is computed with $\mu_{\mathbf{w}} = \sum_{\mathbf{w}_k \in W} \mathbf{w}_k / m$; we obtain the covariance matrix with $\Omega = PP^T$, where $P = [\mathbf{w}_1 - \mu_{\mathbf{w}}, ..., \mathbf{w}_m - \mu_{\mathbf{w}}]$. The variance of the vectors is obtained by computing the norm of the covariance matrix; that is $\|\Omega\| = \sigma_{\mathbf{w}}^2$. The norm is computed with $\|\Omega\| = \sqrt{\lambda(\Omega^T\Omega)}$, where λ is the largest eigenvalue of the matrix $\Omega^T\Omega$.[50]

5. The image is binarized, where the pixels with high chromatic variance are set to 1, otherwise, they are set to 0:

$$b_k = \begin{cases} 1, & \|\mathbf{w}_k - \mu_{\mathbf{w}}\|^2 > \sigma_{\mathbf{w}}^2, \\ 0, & \text{otherwise} \end{cases} \qquad \forall\mathbf{w}_k \in W \tag{12}$$

The pixels that shape the nucleus of the WBCs are those where $b_k = 1$.

6. The binary image is processed with a morphological operator to fill the holes in the WBCs' nucleus, obtaining the pixels of the binary image b_k^*.

7. The pixels of the WBC nucleus are obtained with:

$$\phi_k^{\times} = b_k^* \cdot \phi_k^*, k = 1, ..., m \qquad (13)$$

The flowchart of the segmentation algorithm proposed is shown in Figure 4.

For the HSV colors, the mathematical operations of the step 3 are performed as follows. The vectors of the set $\widehat{\Phi}$ are mapped to the HSV space, obtaining the vectors $\varphi_i = [h_i, s_i, v_i]$, $i = 1, ..., m$. For each vector φ_i, the hue component h_i is extracted to build the set
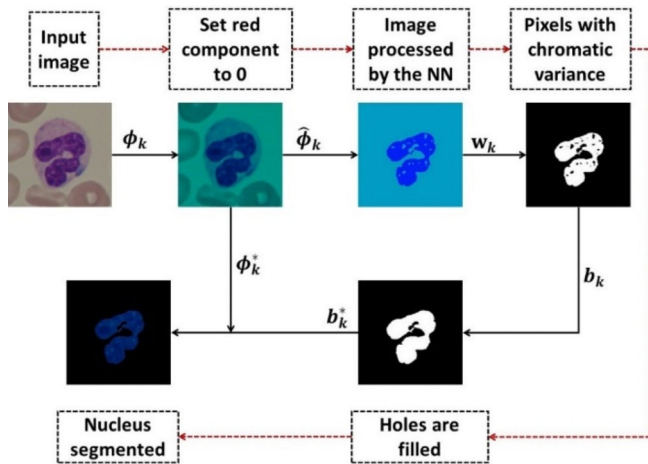
$\Psi = \{\psi_i = [\cos h_i, \sin h_i] | i = 1, ..., m\}$. Analogously, each element of the set Ψ is fed to the NN and the respective weight vector of the winning neuron is placed in the set $W = \{\mathbf{w}_1, ..., \mathbf{w}_m\}$. Finally, the steps 4-7 are performed. Notice that in this case the NN used is the one trained with color samples represented in the HSV space.

4 | EXPERIMENTAL SETUP

For experiments we looked for image databases employed as a benchmark to test WBC segmentation algorithms. Different related works employed their own and private databases, but we found that the most common—and publicly available—datasets are the following: ALL-IDB 2 contains 260 color images of size 257×257, captured using a PowerShot G5 camera; CellaVision consists of 100 color images of size 300×300 and JTSC contains 300 color images of size 120×120 collected by the Jiangxi Tecom Science Corportation.[41] It is important to remark that the brightness and staining conditions in the images of these databases are quite diverse. We employed these datasets to test our approach; these databases and their respective ground truth can be obtained in this repository[*]; an image example for each database and their respective ground truth are shown in Figure 5.

The ground truth images are used to compare them with the resulting images segmented by our method. These ground truth images are hand-segmented by human experts.[41] One main purpose is to advance the efficient automation of this task to diminish human imprecisions and errors.

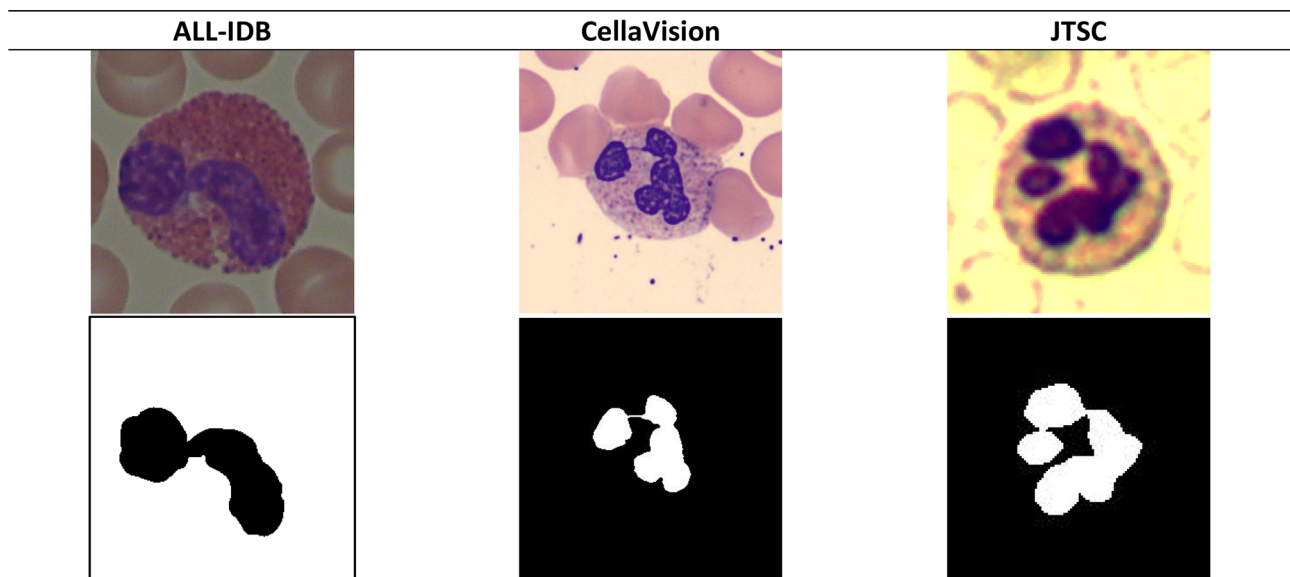**FIGURE 4** Flowchart of the algorithm proposed

FIGURE 5 Images from the databases employed for experiments and their respective ground truth

4.1 | Architecture of neural networks

We use competitive neural networks (CPNNs) and self-organizing maps (SOMs). Two CPNNs are trained with HSV and RGB color samples that we call CPNNHSV and CPNNRGB, respectively. Analogously, two SOMs are trained with HSV and RGB color samples that we call SOMHSV and SOMRGB. The neurons of SOMs are set in a 3×3 array and the CPNNs have nine neurons. All the NNs are trained as mentioned in Section 3.2.

The images of Figure 6 show the color feature maps of the SOMs and CPNNs after training: images (A) and (B) are the feature maps of the SOMs trained with HSV and RGB hue samples, respectively. The images (C) and (D) are the feature maps of the CPNNs trained with HSV and RGB hue samples, respectively. Each square of the NNs is a neuron and its color is the hue that each neuron learned to recognize.

The differences between the CPNNs and SOMs are the architecture and training. The neurons of the SOMs are set in a 2D-array, while the CPNNs are not arranged. Although both NNs are trained with the Kohonen learning rule,[49] in the SOMs the weight vectors of the winning neuron and its neighbor neurons are updated. While in the CPNNs only the weight vector of the winning neuron is updated.

Figure 7 shows examples of images obtained after processing the input images of the first row, with the SOMHSV, CPNNHSV, SOMRGB, and CPNNRGB. As mentioned in Section 3.3, before the images are processed by the NNs, the red component of the colors is set to zero.

In the experimental setup in Section 5, also we perform experiments where images are segmented by computing only the pixels' chromatic variance of the given image, but without process them by the NNs. The experiments using the colors in HSV and RGB are referred as VarHSV and VarRGB, respectively.

4.2 | Evaluation metrics

We evaluated the quality of segmentation by comparing the binary version of the segmented images obtained with our approach and the ground truth. The true positive (TP), false positive (FP), true negative (TN), and false negative (FN) are computed, see Table 1. Note the changes in the second and fourth row.

The performance of the proposal was evaluated using the metrics accuracy (Ac), specificity (Sp), precision (Pr), sensitivity (Se), and kappa index (K):

$$Ac = \frac{TP + TN}{TP + TN + FP + FN} \qquad (14)$$

$$Sp = \frac{TN}{TN + FP} \qquad (15)$$

$$Pr = \frac{TP}{TP + FP} \qquad (16)$$

$$Se = \frac{TP}{TP + FN} \qquad (17)$$

$$K = \frac{Ac - \rho}{1 - \rho} \qquad (18)$$

where

$$\rho = \frac{(TP + FN) \times (TP + FP) + (TN + FN) \times (TN + FP)}{(TP + TN + FP + FN)^2} \qquad (19)$$

According to reference 51, the accuracy level (AL) of the segmented images is classified depending on the value of K as follows:

$$AL = \begin{cases} P, & K \leq 0.2 \\ R, & 0.2 < K \leq 0.4 \\ G, & 0.4 < K \leq 0.6 \\ VG, & 0.6 < K \leq 0.8 \\ E, & K > 0.8 \end{cases} \qquad (20)$$

Here P, R, G, VG, and E indicate Poor, Reasonable, Good, Very Good, and Excellent, respectively.

The dice coefficient (DC), also known as f-score, is employed to compute how correctly a leukocyte is segmented. For each segmented leukocyte k, we obtain DC_k with:

$$DC_k = \frac{2TP}{2TP + FP + FN} \qquad (21)$$

Due to the dataset contains n leukocytes, ADC is defined as the average of all the DC_k computed for the n leukocytes:

$$ADC = \frac{1}{n} \sum_{k=1}^{n} DC_k \qquad (22)$$

A good segmentation algorithm should have a DC value above a specific threshold.[41] Vogado et al.[41] define the true positive rate metric TPR_t for a database as the ratio of the number of leukocytes that achieves $DC_k \geq t$ to the total number of leukocytes.
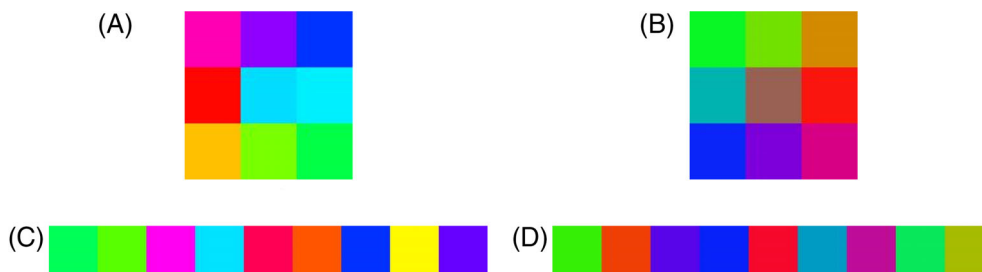
FIGURE 6 Color feature maps: images (A) and (B) show the color feature maps of the SOMs trained with HSV and RGB hue samples, respectively; images (C) and (D) show the color feature maps of the CPNNs trained with HSV and RGB hue samples, respectively
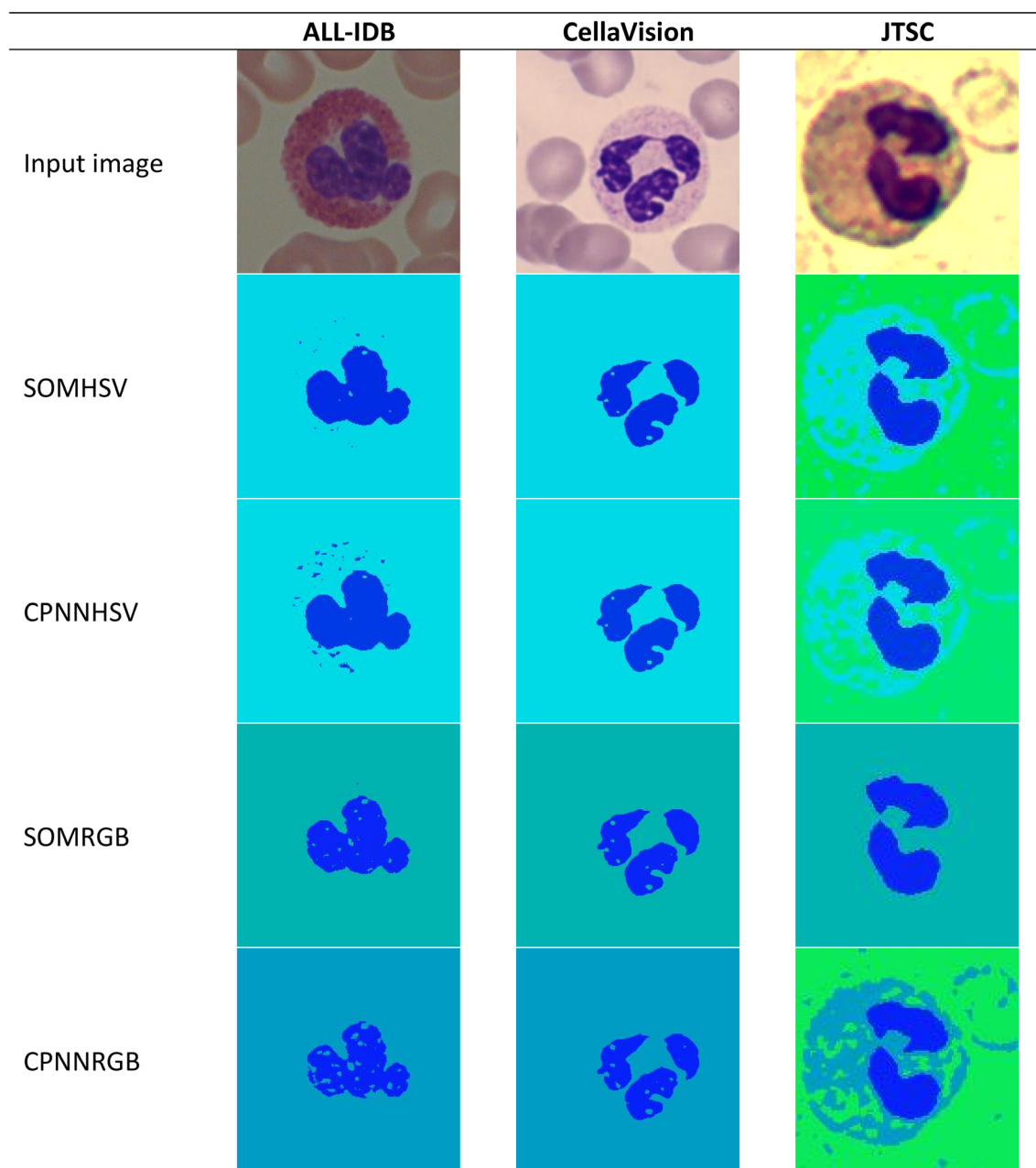

FIGURE 7 Real-world examples of results obtained with HSV and RGB figures using unsupervised NNs

$$\text{TPR}_t = \frac{\#\text{SL}}{n} \qquad (23)$$

Where $\text{SL} = \{k \mid \text{DC}_k \geq t, k = 1, ..., n\}$ and $\#$ denotes the cardinality of the set. Vogado et al.[41] establish that a successful segmentation algorithm should detect at least 80% of the cells with an average DC larger than 0.9; thus, the threshold value is set to $t = 0.9$.

5 | RESULTS AND DISCUSSION

5.1 | Quantitative evaluation

All the images of the ALL-IDB, CellaVision, and JTSC databases were processed. Figure 8 shows image examples of the databases.

Figure 9 shows the resulting images applying our proposal on the images of Figure 8, where the colors are represented in the HSV space. While Figure 10 shows the segmented images using our proposal where the colors are represented in the RGB space.

Tables 2–4 show the quantitative evaluation of our proposal using the metrics described in Section 4.2. In Table 2, the highest specificity and precision values are obtained with CPNNRGB; the highest sensitivity value is obtained with VarHSV. The best accuracy, kappa index, ADC, and TPR values are obtained with CPNNHSV. In all the cases, the K value is greater than 0.8. Therefore, the performance for all the models can be classified as excellent, according to Equation (20).

In Table 3, the highest values for specificity and precision are obtained with the model CPNNRGB. With VarHSV, the highest sensibility value is obtained. The model CPNNHSV obtains the highest values for accuracy, kappa index, ADC, and TPR. Notice that in all the cases $K > 0.8$, so, according to Equation (20), the performances for all the models are classified as excellent.

In Table 4, the model VarHSV obtains the highest sensibility value. The highest precision and specificity values are obtained with SOMRGB. While the highest values for accuracy, kappa index ADC, and TPR are obtained with VarRGB. According to the values of K, the performances of the models SOMHSV, CPNNHSV, SOMRGB, and CPNNRGB are classified as very good class. The performances of VarHSV and VarRGB can be classified as excellent.

The best segmentation performances of the images of the ALL-IDB 2 and CellaVision databases are

TABLE 1 Definition of pixels classified as TP, FP, TN, and FN

	Ground truth	Classified as
TP	WBC	WBC
FP	Background	WBC
TN	Background	Background
FN	WBC	Background
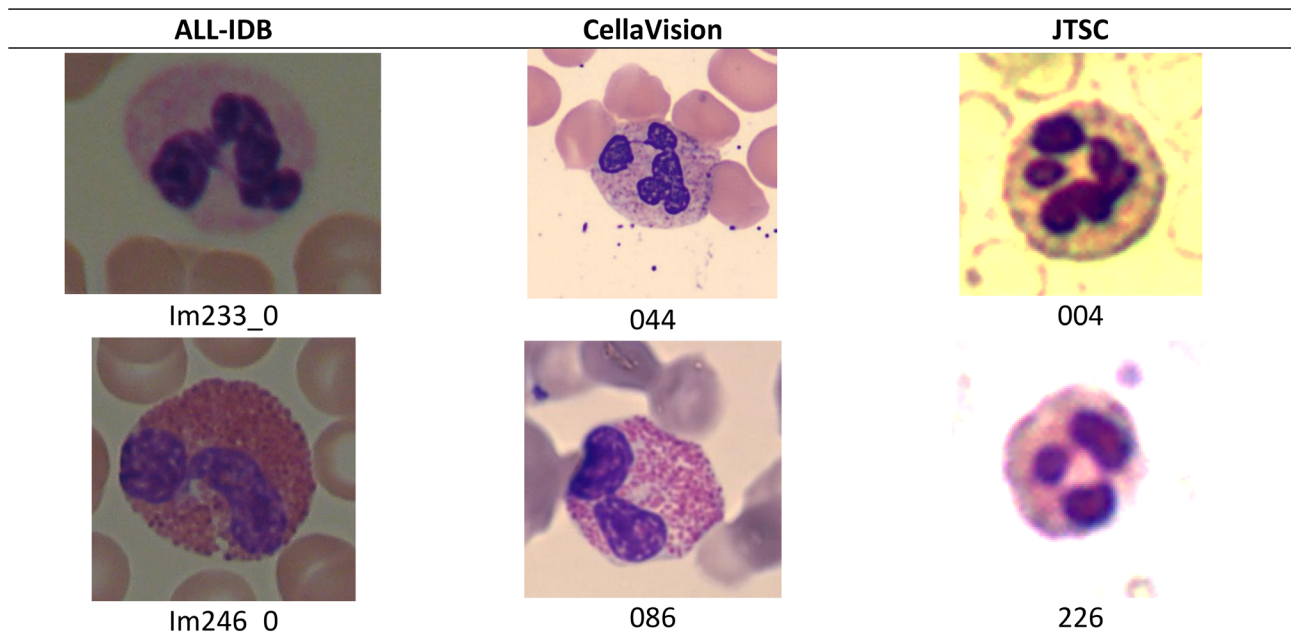
FIGURE 8 Examples of images extracted from databases for experiments; images Im233_0 and Im246_0 are extracted from ALL-IDB 2 database; images 044 and 086 are extracted from CellaVision database; images 004 and 226 are extracted from JTSC database

FIGURE 9   Resulting images by processing the images of Figure 8, using our proposal where the colors are represented in the HSV space

obtained using the CPNNHSV. The kappa index is greater than 0.8; therefore, the performances are classified as excellent. Besides, following the criteria of Vogado et al.,[41] we claim our segmentation approach is successful since the $TPR_{0.9}$ value is greater than 0.8 in both databases.

For the JTSC database, the best performance is obtained with VarRGB. The kappa index is greater
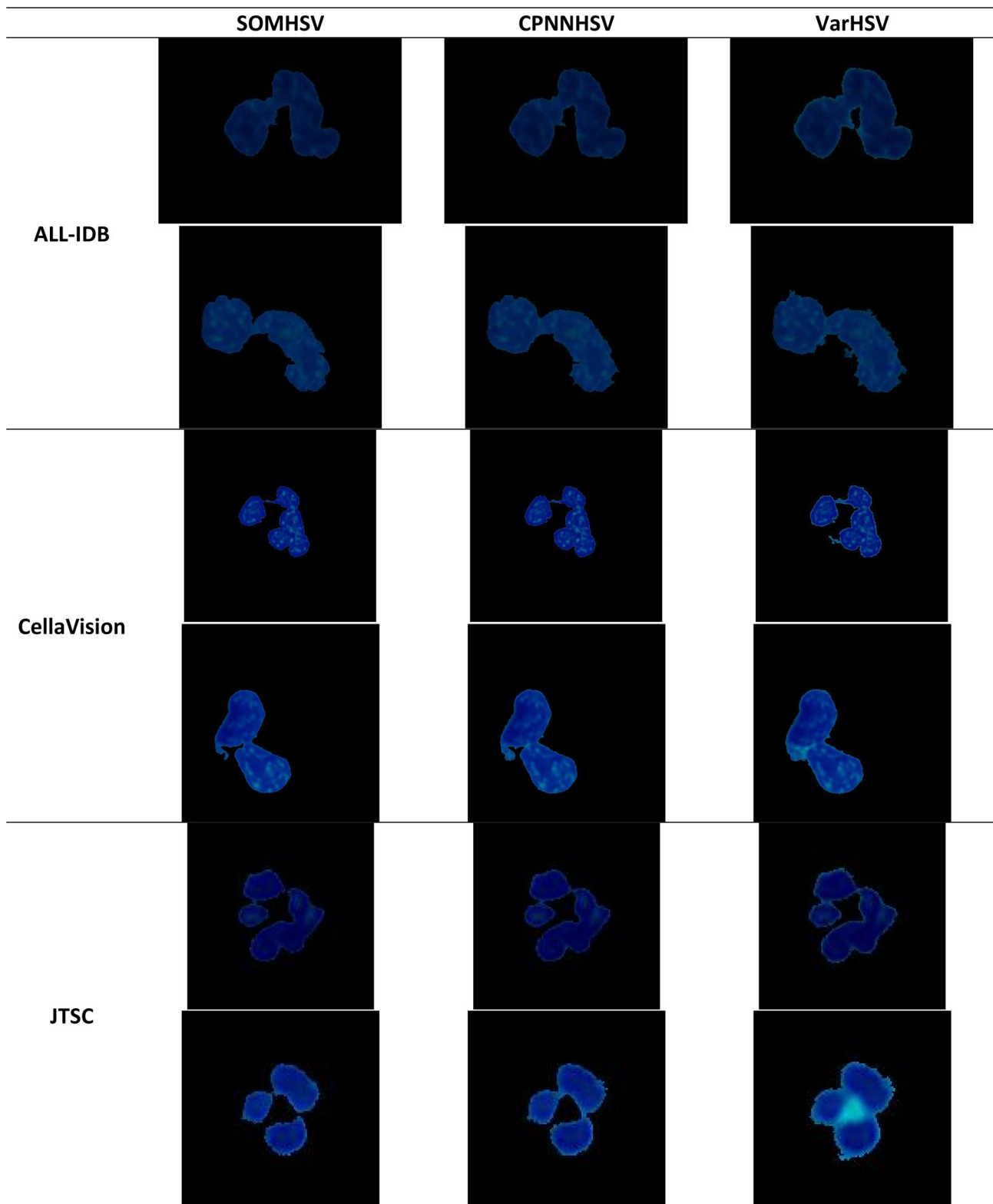
	SOMRGB	CPNNRGB	VarRGB
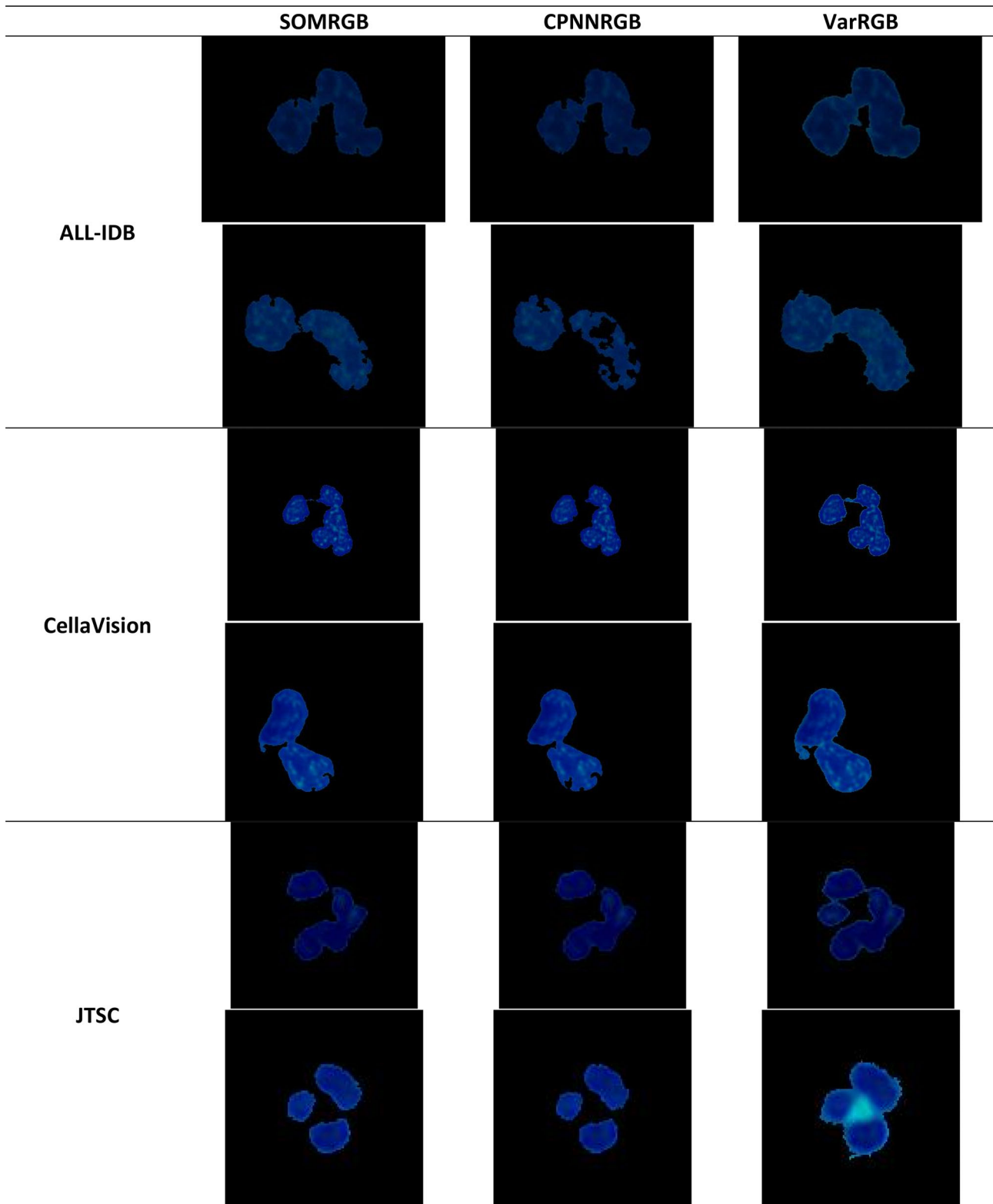
FIGURE 10 Resulting images by processing the images of Figure 8, using our proposal where the colors are represented in the RGB space

than 0.8; therefore, the image segmentation is classified as excellent. But also, the segmentation is successful, according to Vogado et al.,[41] because the $TPR_{0.9}$ value is greater than 0.8. Notice that the values of the metrics obtained with the JTSC database are lower

regarding the values obtained with the ALL-IDB 2 and CellaVision databases.

In the state-of-the-art on image segmentation, usually, the algorithms are validated regarding the ground truth, using the metrics probabilistic random index (PRI),

Method	Acc	Spe	Pre	Sen	K	ADC	TPR$_{0.9}$
SOMHSV	0.9811	0.9899	0.9331	0.9226	0.9169	0.9209	0.8080
CPNNHSV	**0.9832**	0.9866	0.9159	0.9611	**0.9282**	**0.9342**	**0.8560**
VarHSV	0.9773	0.9753	0.8590	**0.9909**	0.9071	0.9007	0.7360
SOMRGB	0.9736	0.9935	0.9516	0.8432	0.8791	0.8736	0.7120
CPNNRGB	0.9634	**0.9959**	**0.9650**	0.7497	0.8235	0.8019	0.6480
VarRGB	0.9816	0.9811	0.8881	0.9849	0.9234	0.9161	0.7800

TABLE 2 Results obtained using the ALL-IDB 2 image database

The best results are in bold.

Method	Acc	Spe	Pre	Sen	K	ADC	TPR$_{0.9}$
SOMHSV	0.9903	0.9961	0.9646	0.9385	0.9460	0.9518	0.8700
CPNNHSV	**0.9920**	0.9941	0.9486	0.9731	**0.9562**	**0.9631**	**0.8800**
VarHSV	0.9709	0.9681	0.7782	**0.9960**	0.8576	0.8884	0.6300
SOMRGB	0.9836	0.9984	0.9837	0.8517	0.9040	0.9040	0.8400
CPNNRGB	0.9761	**0.9991**	**0.9896**	0.7716	0.8542	0.8526	0.7800
VarRGB	0.9892	0.9890	0.9104	0.9908	0.9429	0.9461	0.8400

TABLE 3 Results obtained by using the CellaVision image database

The best results are in bold.

Method	Acc	Spe	Pre	Sen	K	ADC	TPR$_{0.9}$
SOMHSV	0.8971	0.8983	0.5515	0.8882	0.6231	0.7611	0.4333
CPNNHSV	0.9473	0.9491	0.7211	0.9347	0.7840	0.8477	0.4967
VarHSV	0.9808	0.9816	0.8821	**0.9751**	0.9153	0.9259	0.7800
SOMRGB	0.9547	**0.9947**	**0.9465**	0.6706	0.7605	0.7633	0.5633
CPNNRGB	0.8992	0.9015	0.5578	0.8832	0.6274	0.7662	0.4167
VarRGB	**0.9838**	0.9868	0.9110	0.9629	**0.9270**	**0.9388**	**0.8333**

TABLE 4 Results obtained by using the JTSC image database

The best results are in bold.

variation of information (VOI), and global consistency error (GCE).[47,48] Works addressing segmentation of WBCs validate the segmentation algorithms by evaluating the classification at pixel-level of the segmented images. The disadvantage with this approach is that the segmentation cannot be object-based evaluated. The metric TPR$_t$ is subjective, to some extent, since it depends on the threshold t value, which is set intuitively as a proposal by Vogado et al.[41] With the PRI, VOI, and GCE metrics, it is possible to object-based evaluate the segmented images.

Let I and S be the ground truth and the segmentation provided by the algorithm, respectively. The PRI is a measure of the similarity between two data clusters. The PRI is computed with:

$$\text{PRI}(S,I) = \frac{2}{n(n-1)} \sum_{i,j,i<j} p_{i,j}^{c_{i,j}} \left(1 - p_{i,j}\right)^{c_{i,j}} \qquad (24)$$

Where n is the number of pixels, $c_{i,j}$ is a Boolean function: $c_{i,j} = 1$ if $L_i^I = L_j^S$, $c_{i,j} = 0$ otherwise, L_i^I is the label of pixel x_i in the ground truth and L_j^S is the label of pixel x_j in the segmented image, and $p_{i,j}$ is the expected value of the Bernoulli distribution for the pixel pair.

The VOI index measures the sum of loss of information and the gain between two clusters belonging to the lattice of possible partitions in the following way:

$$\text{VOI}(S,I) = H(S) + H(I) - 2F(S,I) \qquad (25)$$

Where H is the entropy $-\sum_{i=1}^{c} (n_i/n)\log(n_i/n)$, n_i being the number of points belonging to the ith cluster, c is the number of clusters, and F is the mutual information between two clusters defined as:

$$F(S,I) = \sum_{i=1}^{c_s} \sum_{j=1}^{c_I} \frac{n_{i,j}}{n} \log \frac{n_i n_j}{n^2} \quad (26)$$

Where $n_{i,j}$ is the number of points in the intersection of cluster i of S and j of I; c_s and c_I are the number of clusters of S and I, respectively.

The GCE computes how a segmented image is viewed as the refinement of other. A measure of error at each pixel x_i can be written as:

$$C(S,I,x_i) = \frac{|R(S,x_i) \setminus R(I,x_i)|}{|R(S,x_i)|} \quad (27)$$

Where $|\cdot|$ is the cardinality, $\setminus$ is the set difference, and $R(S,x_i)$ is the set of pixels corresponding to the region in segmentation S that contains the pixel x_i. The measure enforces all local refinements to be in the same direction, this is defined as:

$$GCE(S,I,x_i) = \frac{1}{n} \min \left(\sum_{i=1}^{n} C(S,I,x_i), \sum_{i=1}^{n} C(I,S,x_i) \right) \quad (28)$$

The ranges of the PRI, VOI, and GCE metrics are $[0,1]$, $[0,\infty)$ and $[0,1]$, respectively. The higher the value of PRI, the better the segmentation is. Similarly, the lower the value of VOI and GCE, the better the segmentation is regarding the ground truth.

Tables 5–7 show the average PRI, VOI, and GCE values obtained by evaluating the segmented images using the ALL-IDB 2, CellaVision, and JTSC databases, respectively.

In Table 5, the best values for PRI and VOI are obtained with the CPNNHSV, while the best value for GCE is obtained with CPNNRGB. Notice that the values obtained with the other approaches are close between them, except for CPNNRGB and VarHSV.

In Table 6, the best values with the three metrics are obtained with CPNNHSV. Notice that the values obtained with the other approaches are close between them, except for CPNNRGB and VarHSV that obtained the lowest performances for PRI, and VOI and GCE metrics, respectively.

In Table 7, the best values for PRI and VOI are obtained with VarHSV, and for the GCE metric, the best value is obtained with SOMRGB. The results obtained with the PRI, VOI, and GCE metrics cannot be compared with related works addressing WBC segmentation because these metrics have not been employed to evaluate the resulting images using other techniques and methods. However, given the results shown in Tables 5–7, it is easy to appreciate that the object-based evaluation similarity between the segmented images and the ground truth is high.

TABLE 5 Average PRI, VOI, and GCE values obtained by evaluating the segmented images using the ALL-IDB 2 database

Method	PRI	VOI	GCE
SOMHSV	0.9644	0.1947	0.0282
CPNNHSV	**0.9677**	**0.1892**	0.0283
VarHSV	0.9571	0.2288	0.0348
SOMRGB	0.9525	0.2169	0.0283
CPNNRGB	0.9362	0.2455	**0.0265**
VarRGB	0.9650	0.1973	0.0292

The best results are in bold.

TABLE 6 Average PRI, VOI, and GCE values obtained by evaluating the segmented images using the CellaVision database

Method	PRI	VOI	GCE
SOMHSV	0.9814	0.1055	0.0144
CPNNHSV	**0.9844**	**0.0944**	**0.0133**
VarHSV	0.9476	0.2293	0.0343
SOMRGB	0.9698	0.1340	0.0151
CPNNRGB	0.9369	0.1708	0.0170
VarRGB	0.9792	0.1180	0.0166

The best results are in bold.

TABLE 7 Average PRI, VOI, and GCE values obtained by evaluating the segmented images using the JTSC database

Method	PRI	VOI	GCE
SOMHSV	0.8517	0.5193	0.0835
CPNNHSV	0.9116	0.3563	0.0561
VarHSV	**0.9634**	**0.1978**	0.0297
SOMRGB	0.9184	0.2950	**0.0300**
CPNNRGB	0.8557	0.5042	0.0795
VarRGB	0.9688	0.1796	0.0266

The best results are in bold.

5.2 | Comparison with state of the art

From experiments, Tables 8–10 show the performance comparison between the results of different methods regarding our proposal on each database. A previous comprehensive performance comparison with methods that use the same databases and metrics we do is in the comparative study of WBC nuclei segmentation.[8] We select the methods that achieved the three highest $TPR_{0.9}$ values with each one of the databases included in each of the tables.

In Table 8, the highest values of specificity and K are obtained in references 32 and 41, respectively; Banik

Method	Acc	Spe	Pre	Sen	K	ADC	$TPR_{0.9}$
Banik et al.[12]	**0.9861**	0.9933	**0.9635**	0.9380	0.9300	0.9400	**0.9115**
Kumar et al.[29]	0.9854	0.9710	0.9189	**0.9873**	0.9339	**0.9426**	0.8960
Nasir et al.[32]	0.9781	**0.9948**	0.9600	0.8870	0.9030	0.9153	0.7307
Hedge et al.[37]	0.9900	-	0.9600	0.9700	-	0.9700	-
Vogado et al.[41]	0.9859	0.9862	0.9124	0.9809	**0.9342**	0.9417	0.8760
CPNNHSV	0.9832	0.9866	0.9159	0.9611	0.9282	0.9342	0.8560

TABLE 8 Comparison of results using the ALL-IDB2 database

The best results are in bold.

Method	Acc	Spe	Pre	Sen	K	ADC	$TPR_{0.9}$
Banik et al.[12]	0.9886	0.9898	0.9175	0.9809	0.9300	0.9400	**0.9000**
Liu et al.[19]	-	-	0.9818	0.8592	-	0.9165	-
Safuan et al.[34]	-	-	0.9781	0.8617	-	0.9161	-
Sarrafzadeh et al.[39]	0.9817	**0.9960**	0.8665	0.9799	0.9111	0.9212	0.7600
Sudha et al.[40]	-	-	**0.9963**	0.8791	-	0.9341	-
Vogado et al.[41]	0.9877	0.8939	0.9788	**0.9975**	0.9254	0.9322	0.8700
Arslan et al.[42]	0.9795	0.9940	0.8698	0.9779	0.9073	0.9176	0.7800
CPNNHSV	**0.9920**	0.9941	0.9486	0.9731	**0.9562**	**0.9631**	0.8800

TABLE 9 Comparison of results using the CellaVision database

The best results are in bold.

Method	Acc	Spe	Pre	Sen	K	ADC	$TPR_{0.9}$
Banik et al.[12]	0.9757	0.9792	0.8763	0.9608	0.8900	0.9100	0.7366
Prinyakupt et al.[27]	0.9611	0.8652	0.8635	0.9779	0.8290	0.8465	0.6066
Kumar et al.[29]	0.9677	0.8186	0.9343	0.9897	0.8474	0.8653	0.4666
Vogado et al.[41]	0.9713	0.8318	**0.9355**	**0.9899**	0.8605	0.8768	0.5233
VarRGB	**0.9838**	**0.9868**	0.9110	0.9629	**0.9270**	**0.9388**	**0.8333**

TABLE 10 Comparison of results using the JTSC database

The best results are in bold.

et al.[12] obtained the highest values for accuracy, precision and $TPR_{0.9}$, while the highest values for sensitivity and ADC are obtained in reference 29. Nevertheless, the values obtained with our proposal CPNNHSV are close. Notice that the results reported by the authors of reference 37 are obtained using only 160 images of the ALL-IDB 2.

In Table 9, the highest values of specificity, precision, sensitivity, and $TPR_{0.9}$ are obtained in references 39, 40, 41, and 12, respectively. Our model CPNNHSV obtains the highest values for accuracy, kappa index, and ADC, but notice that the $TPR_{0.9}$ value our model obtains is very close to the respective value obtained in reference 12. In this table, the references 19, 34, and 40 are also included for comparison, since these references report their performance using the CellaVision database, though they just report values for precision, sensitivity, and ADC.

Reference 15 reports an ADC value of 0.9209, but this value is obtained by processing all the images of the CellaVision and ALL-IDB databases including the images of the Wadsworth Center,[†] without separating the images between databases. In Table 10, the highest values of accuracy, specificity, kappa index, ADC, and $TPR_{0.9}$ are obtained with the model VarRGB. While Vogado et al.[41] obtain the highest values for precision and sensitivity.

Notice that most of the works we employ for comparison use clustering techniques, mainly k-means.[29,32,39,41] But data clustering is influenced by the initial values of the groups' centers and the user must define a priori the number of groups. It means that the segmentation may be different if the given image is processed several times with the same algorithm. Using the NNs we propose as a clustering process, the advantage is that the NNs are trained just once; and they can be employed to segment

the images without training them again. As a result, the segmentation consistency increases.

Note that the lowest metric values are obtained by processing the JTSC database, for our models and the related works too. The explanation is that the quality of images of this database is lower than the images of the ALL-IDB 2 and CellaVision databases, so more difficult to process. On the other hand, the image quality of the ALL-IDB 2 and CellaVision databases is better, so the metric values obtained are higher using these databases. Nonetheless, with our model VarRGB, we obtain the highest K, ADC, and $TPR_{0.9}$ values in the experiments using the JTSC database, as a useful advantage.

5.3 | Chromaticity as a proper characteristic

The methods presented in previous works employ different color spaces to segment the nucleus of WBCs. But the chromaticity is not processed as a feature since the color components are processed separately, uncorrelated. Table 11 shows the color spaces employed to process the color data and the color components used to perform mathematical operations for segmentation in the references we employed to compare our results in Section 5.2.

The methods of Table 11 segment the nuclei by performing mathematical operations between the color components or in a specific color channel, as if they were intensity channels. Therefore, the hue is not processed adequately because the correlation between the color components is lost. Also, mostly, the color channels and mathematical operations are selected intuitively. For instance, in references 27 and 42, the Otsu method, a technique developed to process intensity, is applied to each color component separately. Therefore, the color is processed without being correlated with the color components.

Unlike the previous works, we employ the chromaticity as a proper characteristic; if normalizing the RGB color vectors, just the chromaticity is processed. While in the HSV space, the component H is modeled as unit-length vectors of two elements. In both cases, the hue is processed using matrix operations without losing the correlation between the hue components given the vectorial representation we employ to model the chromaticity.

Notice that several of the methods quoted in Table 11 employ the *k*-means technique. As mentioned before, the clustering techniques tend to create groups with the same size or number of elements; for image segmentation, small parts within the image are not segmented successfully. But also, the performance of the clustering

TABLE 11 Color spaces employed, and color components within mathematical operations for segmentation in related works

Reference	Color space	Components employed and operations performed
Liu et al.[19]	L*a*b*	Histograms of each channel
Prinyakupt et al.[27]	RGB	G values divided by the sum of the average values of the R and B components
Kumar et al.[29]	HSV	*K*-means in H and S components using four clusters, the cluster with smallest red value represents the nucleus region
Nasir et al.[32]	HSI	*K*-means is applied to the H component, then median filter and growing algorithm are applied; the S component is subject to the same sequence of actions
Safuan et al.[34]	RGB, CMYK, HSV, L*a*b*	S-G, C-G, S-C, H-Y; components L*, a*, and b* are used, separately, for image preprocessing
Sarrafzadeh et al.[39]	L*a*b*	*K*-means is used in components a* and b* to divide the image in three clusters. The cluster with the highest intensity component of a* and smallest of component b* is labeled as the nucleus
Sudha et al.[40]	HSV	Edge strength-based location detection and fine segmentation using Grabcut approach are applied to the S component
Vogado et al.[41]	CMYK, L*a*b*	*K*-means is applied to the resulting channel after subtracting channels M and b
Arslan et al.[42]	RGB	Subtraction of channels B and G, negative values are given a value of zero; the image is binarized with the Otsu method and then watershed algorithm is applied

techniques depends on the initial values of the centers. As well note that clustering techniques require, a priori, the number of groups the data (pixels) are grouped; but the convenient number of groups changes depending on the image conditions. With the NN, the number of groups is variable being maximum the number of colors the NN can recognize, so, the number of neurons of the NN.[47] As well, small parts can be segmented using the NN because each pixel is processed independently from the rest of the image. Besides, once the NN is trained, it can be employed to process any image without training it again, unlike the clustering techniques.

Recently, convolutional neural networks (CNNs) to segment the nucleus of WBCs are proposed.[9,11-14,52,53] Each of these works performs experiments using their own and private image databases; they do not employ standard benchmarks and their results cannot be proper compared. Besides, the robustness of the CNN to brightness and staining variations is not discussed because the images they employ are captured under the same illumination and staining conditions. Only[12] use CNN that perform experiments with the same image databases we use. Tables 8–10 show that the results we got are close or even better than the results reported in.[12] It is well known that the computational load of CNN is too high.[52,53] On the opposite, for similar and even improved performances, the computational load of our proposal's implementation is low.

On the other hand, the size of the convolutional neural networks is fixed depending on, partially, the size of the input images. Due to the different sizes of the images in the three image databases employed for experiments, the images must be resized to fit the size of the input layer of the convolutional neural network. Hence, the quality of the image may be degraded, although in reference 12 nothing is mentioned about this aspect. With our approach, image resizing is not necessary.

The CNN trained with the class of supervised algorithms have shown efficiency for image processing. This class of CNN requires a huge amount of diverse representative images to achieve a robust learning so perform the expected task. These CNNs performance strongly depends on the number and kind of training images.[52] Besides, most of the databases are not large enough to train a CNN, and the number of images per WBC class is imbalanced; hence, different works employ synthetic data to train the CNN.[53] All the mentioned processes bring huge load of computational operations.[52,53]

We propose to locate the nucleus of the WBCs by the staining contrast between them and the other elements of the blood smear. The WBC nucleus segmentation select the pixels with high chromatic variance (within a *kind of unsupervised learning*); the segmentation before hue staining and brightness variations is efficient: the

NN is not trained to recognize a specific color but concentrates to enhance the color with high chromatic variance. This flexible method emulates the human perception of color.[48] In addition, the noticeably minor number of operations, regarding the common machine learning methods that use deep or convolutional NN, brings the advantage of quite low computational cost.

Notice that the brightness and staining conditions are different in each of the database. Notably, in the JTSC database the quality of the images is lower than the images of the ALL-IDB 2 and CellaVision ones. Processing the images by the chromatic features the robustness to brightness conditions increases. Besides, by processing the images with the NNs the hue is normalized, and the robustness of staining conditions is improved too. Both improvements are regarding the state-of-the-art methods.

6 | CONCLUSIONS

From our proposed segmentation, more efficient WBC recognition is enabled. This WBC nucleus segmentation in blood smear images uses chromatic features, emulating the human perception of color. The pixels with high chromatic variance are selected to enable the nucleus segmentation. A nine-neuron competitive neural network and a 3×3-neuron self-organizing map were trained offline with hue samples of different colors. As a result, more precisely compute the chromatic variance for WBC recognition. Certain robustness to brightness conditions is achieved by processing the images by chromatic features. Also, processing the hue with the proposed neural networks, an advance on robustness to staining variations is achieved. The results obtained also show that the segmentation is precise and consistent when the colors are processed using the HSV space. Unlike previous works, in our approach the hue components are jointly processed, regarding the correlation between the hue components, within a quite systematic formal sequence. By comparing our results using the accuracy, specificity, precision, sensitivity, kappa index, average dice coefficient, and true positive rate metrics, our proposal obtains competitive results regarding previous related works, and notoriously higher in some cases. The segmentation is classified as excellent regarding the kappa index values obtained from the databases used. Also, our segmentation approach successfully detects more than 80% of the cells with an average dice coefficient larger than 0.9. Considering the results obtained with the object-based evaluation using the probabilistic random index, variation of information and global consistency error metrics, we establish that the similitude between the segmented images and the ground truth is

high. Henceforth, the proposed method is competitive in the state of the art, tested through standard datasets and benchmarks.

DATA AVAILABILITY STATEMENT
The data that support the findings of this study are openly available in gitbhub at https://github.com/zpplmnt/WBC-Nucleus-Segmentation.

ORCID
Farid García-Lamont https://orcid.org/0000-0002-9739-3802

ENDNOTES
* https://github.com/lhvogado/Recent-Computational-Methods-for-White-Blood-Cell-Nuclei-Segmentation-A-Comparative-Study

† http://www.wadsworth.org

REFERENCES
[1] Mishra S, Majhi B, Sa PK. Texture feature based classification on microscopic blood smear for acute lymphoblastic leukemia detection. *Biomed Signal Process Control*. 2019;47:303-311.

[2] Jan Z, Khan A, Sajjad M, Muhammad K, Rho S, Mehmood I. A review on automated diagnosis of malaria parasite in microscopic blood smears images. *Multimed Tools Appl*. 2018;77:9801-9826.

[3] Tsai MH, Yu SS, Chan YK, Jen CC. Blood smear image based malaria parasite and infected-erythrocyte detection and segmentation. *J Med Syst*. 2015;39:118.

[4] Parente J. Diagnosis for white blood cell abnormalities: leukocytes and leukopenia. *Physician Assist Clin*. 2019;4(3):625-635.

[5] Chabot-Richards DS, George TI. White blood cell counts: reference methodology. *Clin Lab Med*. 2015;35(1):11-24.

[6] Global Cancer Observatory, International Agency of Research on Cancer (2020) https://gco.iarc.fr. Accessed May 2021.

[7] Anilkumar K, Manoj V, Sagi T. A survey on image segmentation of blood and bone marrow smear images with emphasis to automated detection of leukemia. *Biocybern Biomed Eng*. 2020;40:1-15.

[8] Andrade AR, Vogado LHS, Veras R, Silva R, Araujo F, Medeiros F. Recent computational methods for white blood cell nuclei segmentation: a comparative study. *Comput Methods Programs Biomed*. 2019;173:1-14.

[9] Hedge RB, Prasad K, Hebbar H, Singh BMK. Comparison of traditional image processing and deep learning approaches for classification of white blood cells in peripheral blood smear images. *Biocybern Biomed Eng*. 2019;39:382-392.

[10] Lopez-Puigdollers D, Traver VJ, Pla F. Recognizing white blood cells with local image descriptors. *Expert Syst Appl*. 2019;115:695-708.

[11] Shahin AI, Guo Y, Amin KM, Sharawi AA. White blood cells identification system based on convolutional deep neural learning networks. *Comput Methods Programs Biomed*. 2019;168:69-89.

[12] Banik PP, Saha R, Kim KD. An automatic nucleus segmentation and cnn model based classification method of white blood cell. *Expert Syst Appl*. 2020;149:113211.

[13] Zhao J, Zhang M, Zhou Z, Chu J, Cao F. Automatic detection and classification of leukocytes using convolutional neural networks. *Med Biol Eng Comput*. 2017;55:1287-1301.

[14] Kutlu H, Avci E, Özyurt F. White blood cells detection and classification based on regional convolutional neural networks. *Med Hypotheses*. 2020;135:109472.

[15] Al-Dulaimi K, Tomeo-Reyes I, Banks J, Chandran V. Evaluation and benchmarking of level set-based three forces via geometric active contours for segmentation of white blood cell nuclei shape. *Comput Biol Med*. 2020;116:103568.

[16] Li Q, Wang Y, Liu H, Wang J, Guo F. A combined spatial-spectral method for automated white blood cells segmentation. *Opt Laser Technol*. 2013;54:225-231.

[17] Wang Q, Chang L, Zhou M, Li Q, Liu H, Guo F. A spectral and morphologic method for white blood cell classification. *Opt Laser Technol*. 2016;84:144-148.

[18] Dorini LB, Minetto R, Leite NJ. Semiautomatic white blood cell segmentation based on multiscale analysis. *IEEE J Biomed Health Inform*. 2013;17(1):250-256.

[19] Liu Y, Cao F, Zhao J, Chu J. Segmentation of white blood cells image using adaptive location and iteration. *IEEE J Biomed Health Inform*. 2017;21(6):1644-1655.

[20] Abdulhay E, Mohammed MA, Ibrahim DA, Arunkumar N, Venkatraman V. Computer aided solution for automatic segmenting and measurements of blood leucocytes using static microscope images. *J Med Syst*. 2018;42:58.

[21] Rezatofighi SH, Soltanian-Zadeh H. Automatic recognition of five types of white blood cells in peripherical blood. *Comput Med Imaging Graph*. 2011;35:333-343.

[22] Ko BC, Gim JW, Narm JY. Automatic white blood cell segmentation using stepwise merging rules and gradient vector flow snake. *Micron*. 2011;42:695-705.

[23] Cao F, Liu Y, Huang Z, Chu J, Zhao J. Effective segmentations in white blood cell images using ϵ-SVR-based detection method. *Neural Comput Appl*. 2019;31:6767-6780.

[24] Zheng X, Wang Y, Wang G, Liu J. Fast and robust segmentation of white blood cell images by self-supervised learning. *Micron*. 2018;107:55-71.

[25] Gupta D, Arora J, Agrawal U, Khanna A, Albuquerque VH. Optimized binary bat algorithm for classification of white blood cells. *Measurement*. 2019;143:180-190.

[26] Ruberto CD, Loddo A, Putzu L. Learning by sampling for white blood cells segmentation. *Int Conf Image Anal Process, LNCS*. 2015;9279:557-567.

[27] Prinyakupt J, Pluempitiwiriyawej C. Segmentation of white blood cells and comparison of cell morphology by linear and naïve Bayes classifiers. *Biomed Eng Online*. 2015;14:63.

[28] Sayed GI, Solyman M, Hassanien AE. A novel chaotic optimal foraging algorithm for unconstrained and constrained problems and its application in white blood cell segmentation. *Neural Comput Appl*. 2019;31:7633-7664.

[29] Kumar PS, Vasuki S. Automated diagnosis of acute lympho-cytic leukemia and acute myeloid leukemia using multi-sv. *J Biomed Imaging Bioeng*. 2017;1(1):20-24.

[30] Cuevas E, Oliva D, Diaz M, Zaldivar D, Perez-Cisneros M, Pajares G. White blood cell segmentation by circle detection using elecromagnetism-like optimization. *Comput Math Methods Med*. 2013;2013:395071.

[31] Cuevas E, Diaz M, Manzanares M, Zaldivar D, Perez-Cisneros M. An improved computer visión method for white blood cells detection. *Comput Math Methods Med*. 2013;2013:137392.

[32] Nasir AS, Mashor MY, Rosline H. Unsupervised colour segmentation of white blood cell for acute leukaemia images. *IEEE Int Conf Imaging Syst Tech*. 2011;5962188. https://doi.org/10.1109/IST.2011.5962188

[33] Nazlibilek S, Karacor D, Ercan T, Sazli MH, Kalender O, Ege Y. Automatic segmentation, counting, size determination and classification of white blood cells. *Measurement*. 2014;55:58-65.

[34] Mohd Safuan SN, Md Tomari MR, Wan Zakaria WN. White blood cell (WBC) counting analysis in blood smear images using various color segmentation methods. *Measurement*. 2018;116:543-555.

[35] Cao F, Cai M, Chu J, Zhao J, Zhou Z. A novel segmentation algorithm for nucleus in white blood cells based on low-rank representation. *Neural Comput Appl*. 2017;28(Suppl 1):S503-S511.

[36] Cao H, Liu H, Song E. A novel algorithm for segmentation of leukocytes in peripherical blood. *Biomed Signal Process Control*. 2018;45:10-21.

[37] Hedge RB, Prasad K, Hebbar H, Singh BMK. Development of a robust algorithm for detection of nuclei of white blood cells in peripheral blood smear images. *Multimed Tools Appl*. 2019;78:17879-17898.

[38] Madhloom HT, Kareem SA, Ariffin H. An image processing application for the localization and segmentation of lympho-blast cell using peripherical blood images. *J Med Syst*. 2012;36:2149-2158.

[39] Sarrafzadeh O, Dehnavi AM, Rabbani H, Talebi A. A simple and accurate method for white blood cells segmentation using k-means algorithm. *IEEE Workshop Signal Process Syst*. 2015;1-6. https://doi.org/10.1109/SiPS.2015.7344978

[40] Sudha K, Geetha P. A novel approach for segmentation and counting of overlapped leukocytes in microscopic blood images. *Biocybern Biomed Eng*. 2020;40:1-10.

[41] Vogado LHS, Veras RMS, Andrade AR, Araujo FHD, Silva RVR, Medeiros FNS. Unsupervised leukemia cells segmentation based on multi-space color channels. *IEEE Int Symp Multimed*. 2016;451-456. https://doi.org/10.1109/ISM.2016.0103

[42] Arslan S, Ozyurek E, Gunduz-Demir C. A color and shape based algorithm for segmentation of white blood cells in peripheral blood and bone marrow images. *J Int Soc Adv Cytometry*. 2014;85(6):480-490.

[43] Ito S, Yoshioka M, Omatu S, Kita K, Kugo K. An image segmentation method using histograms and the human characteristics of HSI color space for a scene image. *Artif Life Robot*. 2006;10(1):6-10.

[44] Paschos G. Perceptually uniform color spaces for color texture analysis: an empirical evaluation. *IEEE Trans Image Process*. 2001;10(6):932-937.

[45] Gonzalez RC, Woods RW. *Digital image processing*. 4th ed. New York, NY: Pearson; 2018.

[46] Garcia-Lamont F, Cervantes J, Lopez-Chau A, Ruiz-Castilla S. Color image segmentation using saturated RGB colors and decoupling the intensity from the hue. *Multimed Tools Appl*. 2020;79:1555-1584.

[47] Garcia-Lamont F, Cervantes J, Lopez-Chau A, Yee-Rendon A. Automatic computing of number of clusters for color image segmentation employing fuzzy c-means by extracting chromaticity features of colors. *Pattern Anal Appl*. 2020;23:59-84.

[48] Garcia-Lamont F, Cervantes J, Lopez-Chau A. Human mimic color perception for segmentation of color images using a three-layered self-organizing map previously trained to classify color chromaticity. *Neural Comput Appl*. 2018;30:871-889.

[49] Kohonen T. The self-organizing map. *Proc IEEE*. 1990;78(9):1464-1480.

[50] Bronshtein I, Semendyayev K, Musiol G, Muehlig H. *Handbook of Mathematics*. Heidelberg: Springer; 2007.

[51] Landis JR, Koch GG. The measurement of observer agreement of categorical data. *Biom*. 1977;33(1):159-174.

[52] Sahlo AT, Kollmannsberger P, Ewees AA. Efficient classification of white blood cell leukemia with improved swarm optimization of deep features. *Sci Rep*. 2020;10:2536.

[53] Vogado L, Veras R, Aires K, et al. Diagnosis of leukaemia in blood slides based on a fine-tuned and highly generalisable deep learning model. *Sensors*. 2021;21:2989.

AUTHOR BIOGRAPHIES

Farid García Lamont received a BS degree in robotics from ESIME-IPN, Mexico City, Mexico, in 2000; in 2004 obtained an MS in automatic control from the Centro de Investigacion y de Estudios Avanzados del IPN (CINVESTAV-IPN), Mexico City, Mexico. In 2010, he received a PhD degree in computer Science from CINVESTAV-IPN. His research interests are pattern recognition, applications of artificial intelligence and robotics.

Matías Alvarado holds a PhD degree in mathematics from the Technical University of Catalonia, Barcelona, Spain, and is a leader researcher in the Department of Computer Science, CINVESTAV-IPN of Mexico. Part of his ongoing research focuses on the segmentation and pattern recognition using chromaticity. Previously he has studied the formal modeling and algorithmic simulation of cancer metastasis and the immune system response; selection strategies for sport team games using Nash equilibrium, vehicle's speed adaptation through machine learning, knowledge management, and epistemic logic.

Asdrúbal López-Chau received a PhD in computer science from the Department of Computer Science at CINVESTAV-IPN, Mexico, in 2013, a MS degree in

computer engineering form CIC-IPN, Mexico, in 2000, and a BS degree in Electronic Engineering from ESIME-IPN, Mexico City, Mexico, in 1997. His research interests include machine learning, computational intelligence, and data mining.

Jair Cervantes received a BS degree in mechanical engineering from Orizaba Technologic Institute, Veracruz, Mexico, in 2001, a MS degree and a PhD from CINVESTAV-IPN, Mexico, in 2005 and 2009, respectively. His research interests include support vector machine, pattern classification, neural networks, fuzzy logic, and clustering.